## Final Technical Report

## Title of Project: Development of Simultaneous Beta-and-Coincidence-Gamma Imager for Plant Imaging Research


## Principal Investigator: Yuan-Chuan Tai



## Grant Number: DE-SC0005157


### Project Objectives

The goal of this project is to develop a novel imaging system that can simultaneously acquire beta and coincidence gamma images of positron sources in thin objects such as leaves of plants. This hybrid imager can be used to measure carbon assimilation in plants quantitatively and in real-time after C-11 labeled carbon-dioxide is administered. A better understanding of carbon assimilation, particularly under the increasingly elevated atmospheric $CO_2$ level, is extremely critical for plant scientists who study food crop and biofuel production. Phase 1 of this project is focused on the technology development with 3 specific aims: (1) develop a hybrid detector that can detect beta and gamma rays simultaneously; (2) develop an imaging system that can differentiate these two types of radiation and acquire beta and coincidence gamma images in real-time; (3) develop techniques to quantify radiotracer distribution using beta and gamma images. Phase 2 of this project is to apply technologies developed in phase 1 to study plants using positron-emitting radionuclide such as $^{11}C$ to study carbon assimilation in biofuel plants.

### Project Results

We have completed all 3 specific aims of the phase 1 work and initiated new plant imaging research in phase 2. Outcomes from individual aims are reported below.

**1. Develop a hybrid detector that can detect beta and gamma rays simultaneously**

Initial proof-concept development of a hybrid phoswich detector that can detect both beta particles and gamma rays from positron-emitting radionuclides was published in the publication list #1. Using the same design, we developed a second generation detector for detecting beta and gamma rays simultaneously. It consists of a sheet of plastic scintillator (BC-404 from Saint Gobain, 48 x 48 x 1 $mm^3$ in dimension), a LYSO crystal array (48 x 48 elements of 1x1x10 $mm^3$ each), a sheet of acrylic 48 x 48 x 1.5 $mm^3$ (as a light diffuser) and a multi-channel PMT (Hamamatsu H8500) (Fig. 1). The plastic scintillator serves as a beta detector and is insensitive to 511 keV gamma rays due to its low density. The LYSO crystal array can detect gamma rays effectively and also serves as a coherent light guide to couple scintillation light from the plastic scintillator to PMT. A 25 μm aluminum foil is used to wrap the front surface of the phoswich detector to keep it light tight without significant attenuation of the beta particles.

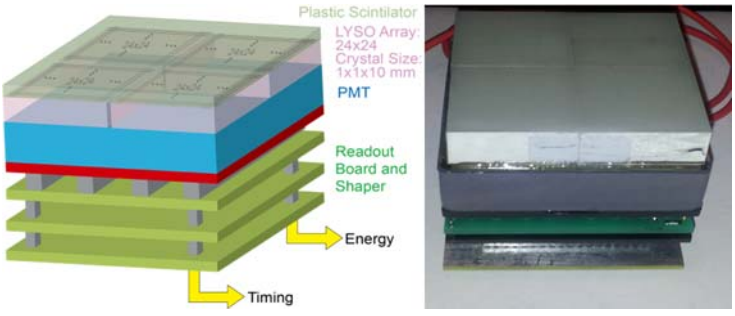


Figure 1. A schematic drawing (left) and a photograph (right) of the phoswich detector that was developed for the proposed hybrid imager

Because the plastic scintillator and LYSO crystal have distinct decay constants (2.1 ns for plastic scintillator and 40 ns for LYSO, as shown in Fig. 2L), pulse-shape discrimination technique that samples detector waveforms at 2 different times can be used to differentiate beta and gamma ray events (Fig. 2M). We used a Sallen-Key band pass filter to condition the PMT signal. The filtered pulse height is

proportional to the total input charge while the pulse width is proportional to the input pulse length. A 150 ns timing constant is chosen for the circuit so that the filtered pulse is optimized for the digitizer used in the system (sampled at 105 MHz). If we plot the digitized signal amplitudes at T1 and T2 as a scatter plot, events from the plastic scintillator will cluster in the region left to the threshold 1, while events from the LYSO crystals will cluster in the region above the threshold 2 (shown in Fig. 2R). Using the ratio of the digitized signal amplitudes at 2 pre-determined time points relative to the constant-fraction-discriminator (CFD) trigger time, we can implement a classifier in field programmable gate array (FPGA) to identify the origin of the events in real time.

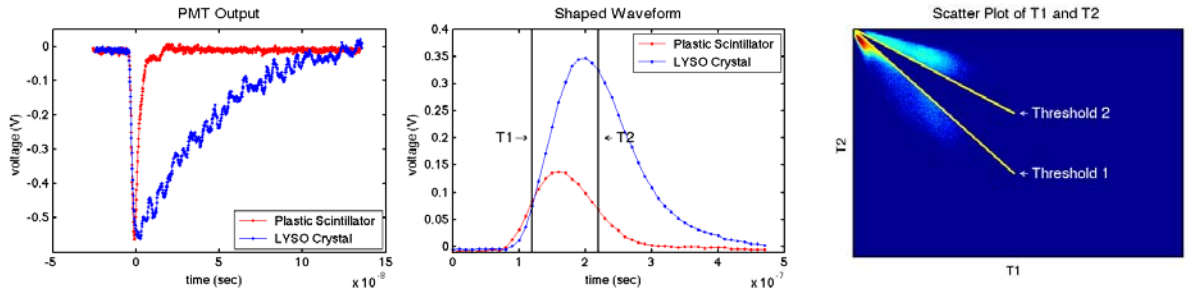


Figure 2. (L) PMT output showing different waveform characteristics when the signal is originated from the plastic scintillator and the LYSO crystals. (M) Integrated PMT signals showing different rise and decay time constants of the 2 types of event that can be differentiated by pulse shape discriminator. (R) Classifier that was used to identify plastic scintillation events and LYSO events.

**2. Develop a hybrid imager for simultaneous beta-and-coincidence-gamma imaging in real-time**

The hybrid imager (Fig. 3) consists of (1) a phoswich detector described above, (2) a gamma detector made of the same type of PMT and LYSO array, (3) NIM electronics (fan-in-fan-out and CFD), and (4) a 16-channel waveform sampling analog-to-digital converter (ADC) system (VHS-ADC from NUTAQ Inc).

Figure 3. The hybrid imager consists of a gamma detector, a phoswich detector, NIM electronics, and an ADC system.

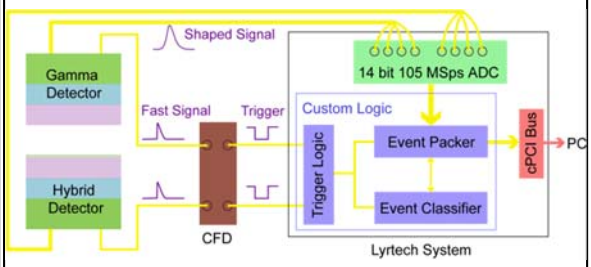


Figure 4. Functional diagram of the imager: PMT outputs are shaped before digitization. Fast signals were used to generate trigger for ADC. Event processing and classification logics are implemented in the on-board FPGA.

The PMT outputs from detectors 1 and 2 are split, with the fast signals sent to the CFD module to create triggers for the ADC system, while the shaped signals digitized by the waveform sampling ADC system. Real-time event classifier (described above), implemented with custom logics in the on-board FPGA, determines the type of event (beta vs. gamma) from the phoswich detector. Beta events were sent to the host computer to form beta image, while gamma events are compared to the singles events from the upper PET detector for coincidence detection. Coincidence events between the two LYSO detectors were

recorded as list mode data and reconstructed to form a PET image using focal plane reconstruction method. Figure 4 shows the functional diagram of event processing in the system.

*Intrinsic spatial resolution of the imager*

A point source phantom was used to characterize the intrinsic spatial resolution of the imager for both beta and coincidence gamma images. The phantom was created by depositing $^{18}$F solution onto a piece of 80 μm plastic film in a point grid pattern shown in Fig. 5L, and subsequently covered by a layer of 20 μm protective tape. The size of the $^{18}$F point sources was < 1 mm, hence the source dimension was not compensated when evaluating the intrinsic spatial resolution. In order to minimize the beta energy loss as well as the source-to-detector distance, the 20 μm protective tape side of the phantom was facing the phoswich detector. A beta and a coincidence gamma image were acquired simultaneously. Profiles were extracted from the beta and coincidence gamma image to evaluate the intrinsic spatial resolution of the system. Results show that the beta and coincidence gamma images have an intrinsic spatial resolution of 2.45 and 1.45 mm FWHM, respectively. It should be noted that these results correspond to the intrinsic d performance. The actual image resolution of an object depends on the object location and thickness which will be characterized separately.

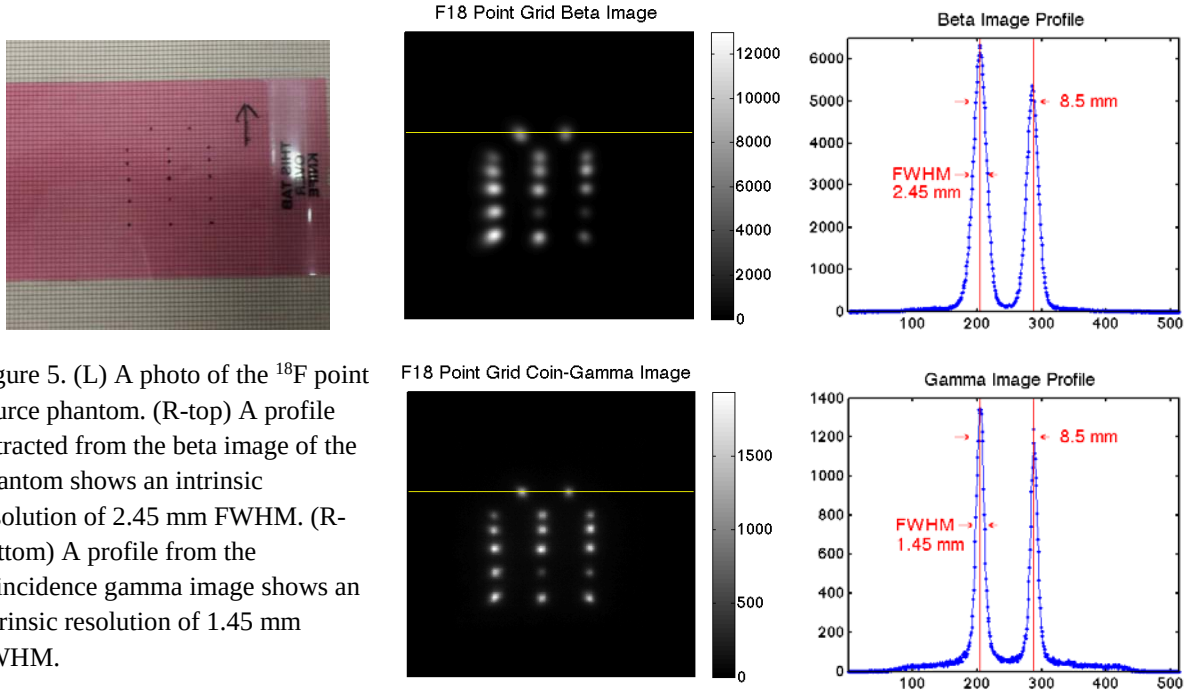


Figure 5. (L) A photo of the $^{18}$F point source phantom. (R-top) A profile extracted from the beta image of the phantom shows an intrinsic resolution of 2.45 mm FWHM. (R-bottom) A profile from the coincidence gamma image shows an intrinsic resolution of 1.45 mm FWHM.

*Characterization of system response versus object thickness and distance*

It was well understood that the object density and thickness will affect the fraction of positrons that can escape from the object, as well as the efficiency of positron annihilation within the object. Furthermore, the system response may not be a constant as the object-to-detector distance changes. We characterized the image resolution and system sensitivity as a function of object thickness and distance because a real leaf usually has non-uniform thickness and may not be completely flat on the detector surface.

A phantom was created by depositing two $^{18}$F solution droplets onto a thin acrylic sheet that was supported by a translation stage that can move the phantom up and down above the phoswich detector surface. We

used plastic tape to mimic leaf tissues and created phantoms of different thickness that ranges from 0 to 0.9 mm in 0.15 mm increments. The source height was adjusted using the translation stage from 0 to 2.75 mm above the phoswich detector surface (Fig. 6L) in 0.25 mm increments. At each source height, we acquired beta and coincidence gamma images. The image resolution was measured from profiles extracted from the corresponding images, while the overall system sensitivity was estimated from the total counts in the individual images. Figure 6R shows an example set of beta images that was acquired using a phantom of 0.15 mm thick at different source-to-detector distances.

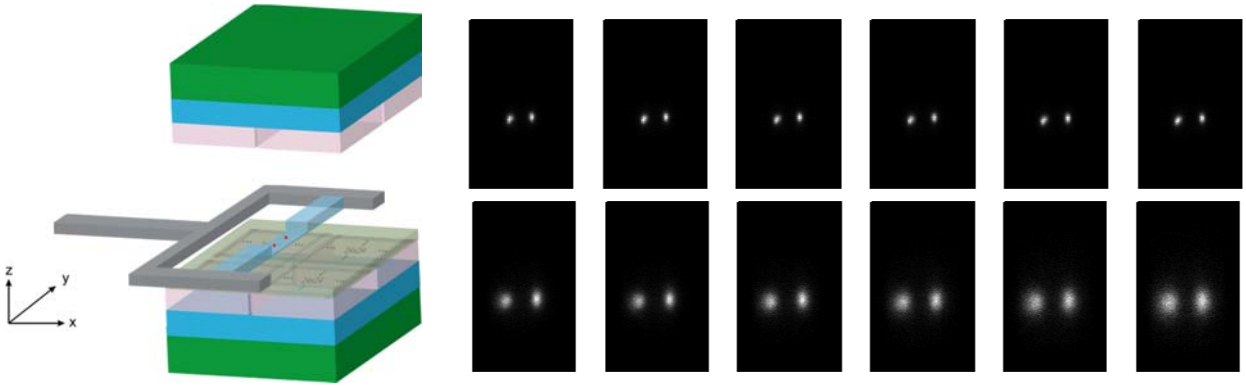


Figure 6. (L) A drawing showing the setup for characterizing the image resolution and system sensitivity as a function of source-to-detector distance and object thickness. (R) An example set of beta image acquired using a phantom of 0.15 mm thick at different source-to-detector distances.

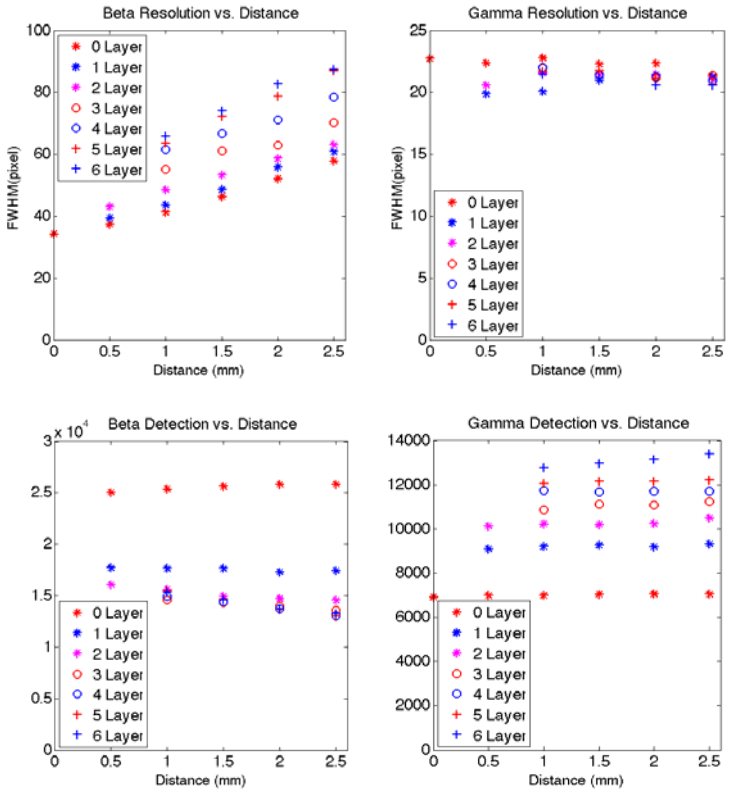


Figure 7. (Top) Image resolution of the beta (L) and coincidence gamma (R) images as a function of source-to-detector distance for different object thickness. Each layer of tape is 0.15 mm thick.

(Bottom) Overall system sensitivity of the beta (L) and coincidence gamma (R) images as a function of source-to-detector distance for different object thickness.

Fig. 7-Top shows that the beta image resolution degrades quickly when the source-to-detector distance increases. The increase in object thickness also contributes to the degradation of beta image resolution. In contrast, the coincidence gamma image resolution is relatively insensitive to the source-to-detector distance and object thickness. Fig. 7-Bottom shows that the beta detection efficiency drops exponentially when the object thickness increases, while at the same time the coincidence gamma detection efficiency increases exponentially following the same trend. One interesting observation is that the beta event rate stopped decreasing after two layers of tapes were applied, while the coincidence gamma event rate kept increasing all the way through the sixth layer. This could be explained by the fact that the imaging system is triggered only by events with sufficient energy due to the use of CFD. The majority of beta particles will have low residual energy when they reach the phoswich detector after passing through more than 2 layers of tapes and the light shield material above the detector. As a result, the beta event rate no longer decreases when more than 2 layers of tapes were applied. The recorded events are likely due to LYSO's internal radiation and the annihilation gamma rays that interact with the plastic scintillator. In contrast, the probability of positron annihilation increases when more layers of tapes were applied as long as the total thickness does not exceed the maximal positron range of the radionuclide.

*Linearity of the beta imager*

Since the plastic scintillator is not pixelated, the beta imager behaves similarly to a conventional gamma camera that is made of a monolithic NaI(Tl) crystal read out by multiple PMT. We tested the linearity of the beta imager by moving a $^{64}$Cu line source across the detector surface with a high resolution translation stage. The physical position of the line source was correlated with the line source location in the beta image. We repeated the measurement for sources at different source-to-detector distances. A high order polynomial function was fitted to the data and used for linearity correction. The polynomial fit was found to be independent of the source-to-detector distance, suggesting that the same linearity correction is applicable regardless of the leaf location. Figure 8 shows the experiment setup and the linearity of the system after the same correction was applied to sources at different heights. The results clearly demonstrated an imager with good linearity in the central region of the imaging field of view, regardless of the source height.

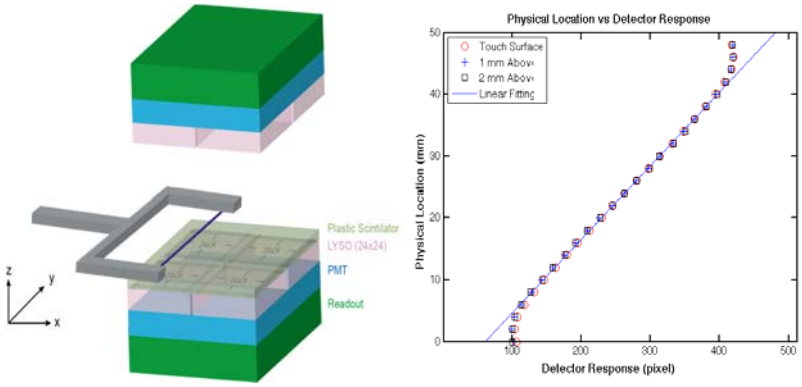


Figure 8. (L) A drawing showing the setup for testing the linearity of the beta imager. (R) For the central region of the beta imager, the system response is very linear and independent of the source-to-detector distance.

*Initial plant image experiment*

To test the hybrid imager's function with a real plant, we radiolabeled a small cucumber plant with $^{11}CO_2$ using a custom labeling chamber (Fig. 9L). 370 MBq of $^{11}CO_2$ was injected into the chamber. The plant was well illuminated to induce photosynthesis. 15 minutes uptake time was allowed for radiolabeling of $^{11}CO_2$. At the end of the labeling, normal air was flushed into the chamber to push all the residual radioactive gas out to a soda lime trap. A leaf was imaged by the hybrid imager to acquire beta and coincidence gamma images simultaneously. Figure 9 shows the photographs of the labeling chamber (left) and a leaf on top of the phoswich detector (right). Figure 10 shows the beta image (left) and coincidence gamma image (right) simultaneously measured by the hybrid imager. The beta image shows high uptake along the peripheral regions where the leaf is thin, while the coincidence gamma image shows uptake throughout the leaf. The thickest parts of the leaf near the central veins show clear mismatch pattern between the beta and coincidence gamma images. These results demonstrate the deficiency of both imaging modalities. That is, neither of these 2 types of images represents a quantitative measurement of the true activity distribution within a leaf. Simultaneously acquired beta and coincidence gamma images from our hybrid imager will allow us to estimate the carbon assimilation in plant leaves in real time after $^{11}CO_2$ labeling more quantitatively.

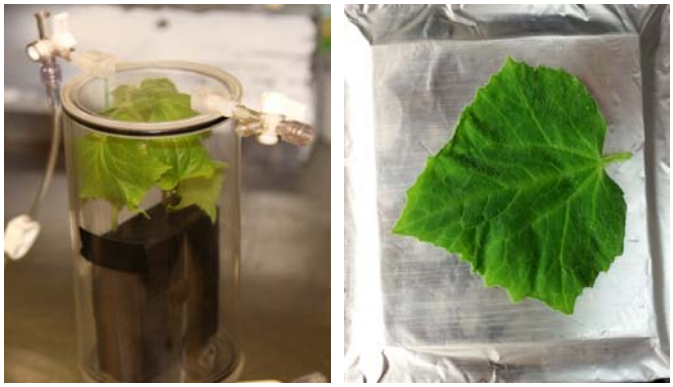

Figure 9. (L) Photographs of a plant labeling chamber with a cucumber plant inside. (R) A radiolabeled leaf on top of the phoswich detector being imaged by the hybrid imager.

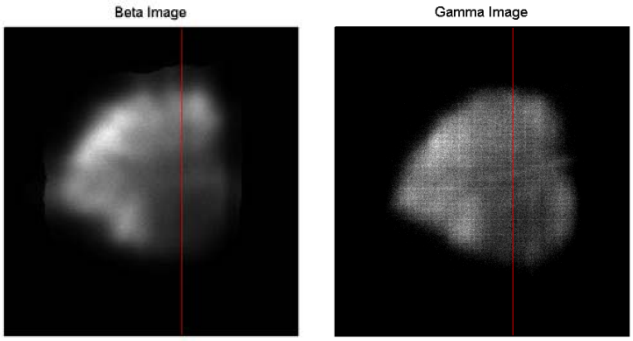


Figure 10. The beta image (L) and the coincidence gamma image (R) of a cucumber leaf after it is radiolabeled by $^{11}CO_2$.

### 3. Develop techniques to quantify radiotracer distribution using beta and gamma images

With the distinctly different resolution and sensitivity characteristics of the beta and coincidence gamma images from the hybrid imager (as reported in section 2 above), there is not a simple analytical solution that

can estimate the true activity distribution within a leaf from the beta and coincidence gamma images directly. The solution will depend on not only the measured beta and coincidence gamma images, but also the thickness of the leaf and the leaf-to-detector distance. The physical model that we derived for this unique system follows the following derivation:

Beta and gamma measurements are separately sorted into data arrays. Beta data, namely $d_\beta$, is sorted by (Anger Logic) weight-positioning the plastic scintillator events from the phoswich detector. Similarly coincidence-gamma data, $d_\gamma$, is sorted by (Anger Logic) weight-positioning the LYSO crystal events from both phoswich and gamma detectors. For gamma reconstruction, the standard PET system matrix is used. We propose a separate system matrix for beta, $H_\beta$. In our imaging set-up, since positrons move within three media: leaf (object), air gap (between the leaf and the hybrid detector's plastic scintillator), and the plastic scintillator, beta system matrix consists of three components: medium-dependent component ($H_3$), air-gap-dependent component ($H_2$), and plastic scintillator point spread function ($H_1$), respectively. Therefore the overall beta system matrix is modeled using a factored matrix approach: $H_\beta = H_1 \bullet H_2 \bullet H_3$.

For the medium-dependent component $H_3$, we used the model that has been developed by Derenzo and validated by Levin and Hoffman by Monte Carlo calculations. That is, the positrons undergo a random walk in water equivalent media, and that the ratio of number of positrons that survive passing through a particular distance from the origin of decay to the total number of positrons as a sum of two exponential functions of that distance. Based on experimentally acquired data from a $^{18}F$ point source embedded between multiple layers of scotch tapes to mimic leaves of different thickness, we can fit the beta-surviving probability as a function of medium thickness, and then estimate the Gaussian kernels of the system matrix component $H_3$ with two exponential terms. Figure 11 shows the experimental results fitted to estimate the two exponential function.

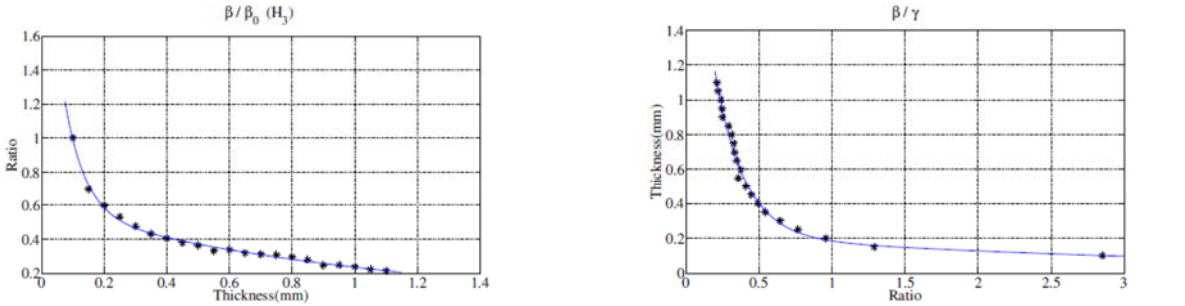


(a) The normalized ratio of beta image value versus medium thickness.

(b) The medium thickness versus the ratio of beta image value over gamma image value.

Figure 11. Calibration experiment. The experimental measurements are fitted to a sum of two exponential functions, i.e. $y = ae^{bx} + ce^{dx}$.

For the air-gap-dependent component $H_2$, we try to model the escaping positrons move in the air gap between the leaf and the plastic scintillator. Inverse square law and obliquity can best model positron's movement in the air because of relatively low density of air. Define $[H_2]_{kj}$ as the probability of a surviving positron from the j-th object voxel to be incident at the k-th unit, namely $u_k$, on the top of the plastic scintillator as an intermediate plane, namely K ($k \in K$).

$$[H_2]_{kj} \propto \left(\frac{1}{R_{kj}^2} \cdot cos\theta_{kj}\right)$$

Where R is the distance between the j-th object voxel and the k-th unit on the top of the plastic scintillator, while θ is the angle between them.

For the system matrix component that relates to the point spread function of the plastic scintillator $H_1$, we used a piece of beta data from an $^{18}F$ point source less than 1 mm in diameter and of almost zero medium thickness. Typically the air gap is very thin ($H_2$ is nearly diagonal), $H_3$ has been shown not to add extra blurring (presumably diagonal), therefore the primary factor of blurring is the scintillators response. A weighted sum of two 2D Gaussian kernels, best fits our experimental beta data.

To estimate the radioactivity distribution in leaves quantitatively, we use both positron and coincidence-gamma measurements, and a complete inclusion of beta system matrix i.e. $H_\beta = H_1 \bullet H_2 \bullet H_3$. Upon the common emission tomography statistical image reconstruction framework (Shepp and Vardi 1982, Lange and Carson 1984), we built that of our joint β–γ image reconstruction in which a weighted sum of a gamma and a beta likelihood function is maximized under non-negativity constraints. The derivation can be seen in the publication list #2.

We conducted a validation study that consisted of the following steps: A tomato plant was labeled by 6.5 mCi of $^{11}CO_2$ injected into a sealed labeling chamber (~1 liter). After the labeling process (10 minutes) the activity was flushed out for 10 minutes with fresh air. Then one of the labeled leaves was detached and used for two imaging experiments: 1) PET imaging by a Plant PET Imager, and 2) Imaging by the Simultaneous Beta-Gamma Imager. In PET imaging, the leaf was sandwiched between two 3 mm thick layers of plastic and submerged into water, to effectively eliminate positron escape. The image from PlantPET Imager serves as our “Ground Truth” image for quantitative performance evaluation of the Simultaneous Beta-Gamma Imager and therefore the PET image must be quantitative. Figure 12 shows the ground truth image as reconstructed using the ML-EM algorithm with image voxel size of 0.8 mm x 0.8 mm x 0.8 mm. Due to the use of large LSO crystals in the Plant PET scanner and larger voxel size, this image has lower resolution compared to images from Simultaneous Beta-Gamma Imager but it has better quantification because of positron escape elimination.

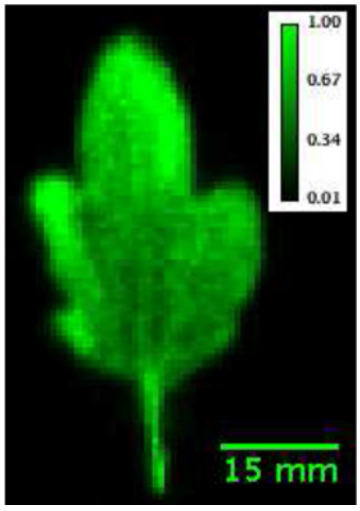


Figure 12: Tomato leaf image obtained from a PET scanner with the leaf sandwiched by two plastic sheets to serve as the "ground truth" for quantitation.

In Beta-Gamma imaging we placed the leaf on the surface of the phoswich detector acquired simultaneous data from the leaf for 3 hours. The simultaneous positron-and-coincidence gamma data collected by the Simultaneous Beta-Gamma Imager was used for beta alone, gamma alone, and joint beta and gamma reconstruction schemes. The images are shown in Figure 13.

Subjectively, among the images in Figure 13, the joint beta and gamma reconstruction image (Figure 13c) resembles the ground truth image in Figure 12 better than either of the two separate reconstruction images, i.e. beta alone and gamma alone (Figures 13a and 13b, respectively). The beta image captures the dominant $^{11}CO_2$ uptake in the leaf but has relatively lower resolution. Also it fails to capture the structural features on the midrib and the $^{11}CO_2$ uptake in the veins as opposed to the gamma image in which the veins are visible. The gamma image gives a misleading indication of how the true radioactivity is distributed in the relatively thin regions of the leaf such as the top right edge and the side

lobes. The joint beta and gamma image captures both the structural features and $^{11}CO_2$ uptake distribution in the leaf.

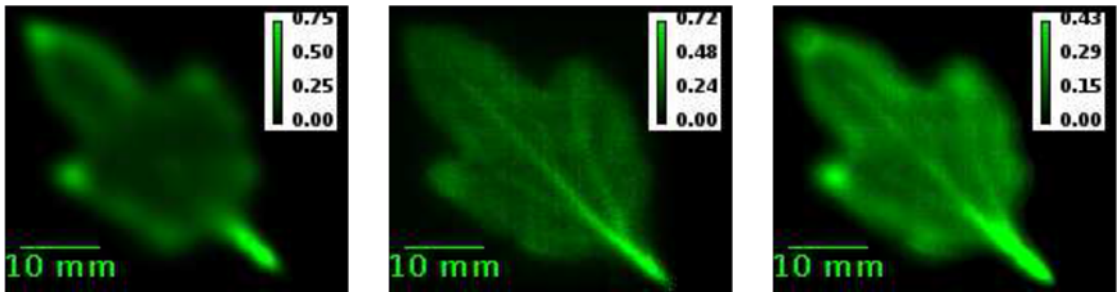


(a) Beta alone reconstruction (b) Gamma alone reconstruction (c) Joint beta and gamma reconstruction

Figure 13: Tomato leaf images reconstructed from simultaneous positron and coincidence-gamma data collected by the Simultaneous Beta-Gamma Imager, using ML-EM algorithm with an image voxel size of 0.25 x 0.25 x 1 $mm^3$. Color bars have unit of normalized value.

A more objective assessment of the image quantification of the jointly reconstructed image can be achieved by using the structural similarity (SSIM) approach, and the results are shown in the publication list #2 in greater details.

**4. Summary of Phase 1 work**

We successfully developed a Simultaneous Beta and Coincidence-Gamma Imager, the corresponding physics model for the imaging system, and an image reconstruction framework to achieve quantitative images of radioactivity distribution in thin objects such as plant leaves. This work allows us to image leaves of plants quantitatively with important radiotracers such as $^{11}CO_2$ to study carbon assimilation, translocation, and utilization in energy crops. This new capability will enable new research initiatives to meet the DOE missions that address the global climate change and renewal energy sources through advanced plant research.

**5. Phase 2 work of new initiatives in molecular plant imaging research**

In addition to the simultaneous beta and coincidence-gamma imager described above, we also developed a new approach that uses Cherenkov Luminescence Imaging (CLI) to image radiotracers in plant. The positrons emitted from $^{11}C$ following radioactive decay have sufficient energy to induce Cherenkov radiation (CR) as the beta particles travel through the medium (leaf or plant tissues). For CR originated from $^{11}C$ in leaves, the signal intensity is orders of magnitude lower than the fluorescence signal emitted by leaves after they are exposed to light. We demonstrated the feasibility of in vivo CLI of $^{11}C$ in leaves by blocking off the intrinsic fluorescence signal using a light shield, followed by inducing more CR signal with a transducer. Figure 14 illustrates (a) the setup for radiolabeling a young plant with $^{11}CO_2$; (2) a schematics showing the setup to block off fluorescence light from the leaf using a thin layer of plastic light shield and the placement of a transducer above the light shield to induce CR for imaging; (c) using an optical imager (PerkinElmer IVIS Lumina II XR), we acquired an optical image (color) of the leaf covered by a light shield and fused it with the white-light image (gray scale) to demonstrate complete block-off of the fluorescence signal from the leaf; (4) CLI image (color) induced by a transducer above the light shield; the CLI image was then fused with the white-light image (gray scale) of the leaf/light-shield; (e) CLI image of the same leaf after it was detached from the plant. The leaf was flipped relative to the leaf position/orientation in Figure 14d. The *in vivo* and *in vitro* CLI images are very similar to each other, demonstrating the feasibility of in vivo CLI imaging for measuring $^{11}C$ concentration in a thin leaf.

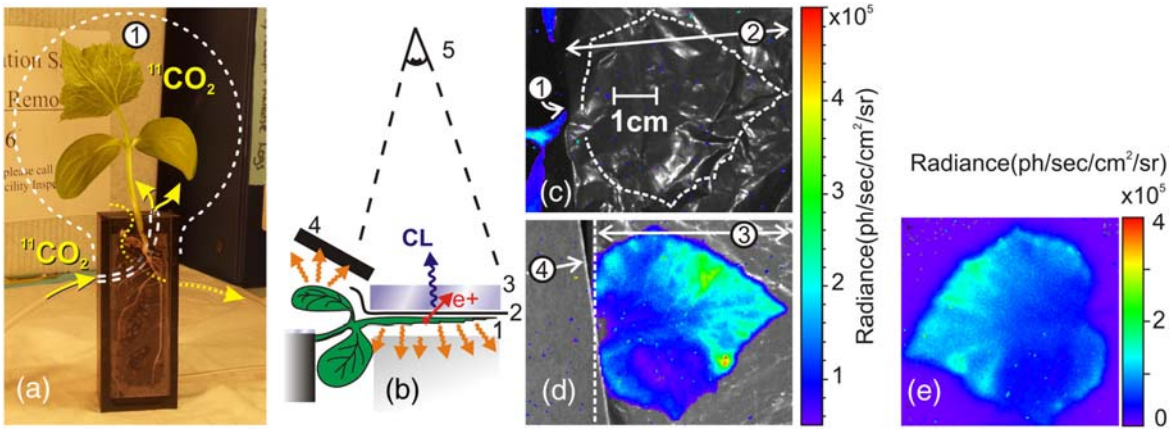


Figure 14. Plant imaging experiment: (a) a young cucumber plant labeled with $^{11}CO_2$ gas (370 MBq for 15 min in ~1 L chamber); (b) CLI setup: a thin black plastic sheet (2) blocks phosphorescent light from the imaged leaf (1); an acrylic transducer 12 mm thick (3) is placed over the leaf; an additional black paper screen (4) blocks phosphorescent light outside the imaging field of view (FOV); (5) is a CCD camera; (c) CLI of the leaf (1) covered by thin black plastic sheet (2) without transducer; (d) CLI of the same leaf with transducer (3); (e) CLI of detached and flipped leaf. The optical grease Bicron BC 630 was used between (2) and (3) to press the plastic sheet to the leaf surface and fill the gap between the flat transducer and the plastic sheet. (d) and (e) are obtained 18 and 36 min after the labeling.

Encouraged by this promising result, we further investigated the feasibility of using CLI to study the transportation and allocation of carbon in plants using $^{11}C$ labels. We first grew a plant using a small plastic container that has a transparent glass window on a side, similar to the one shown in Figure 14a. We radiolabel the leaves of the plant with $^{11}CO_2$. We imaged the plant using the same optical imager at 1h and 6h post radiolabeling. Both the 1h and 6h images show strong fluorescence signals in the leaves because we had to use a flash light to get the standard photographic images (Figure 15c), which activated the fluorophore in the leaves. However, there is no signal in the roots in the 6h image, demonstrating that the signals in the roots at 1h time-point are not fluorescence signal but CLI signals. Figure 15d is a zoom-in version of the CLI image of the root section demonstrating the feasibility of CLI to provide high-resolution image of $^{11}C$ distribution in roots. The estimated image resolution of the CLI for measuring $^{11}C$ distribution in transparent media is approximately 600 micron full-width-at-half-maximum. This is significantly higher than standard PET scanners designed for small animal or human imaging applications and will offer new opportunities to study photosynthates and the carbon translocation in plants. More details on the characterization of CLI images for thin objects or objects in transparent media can be found in publication list #3.

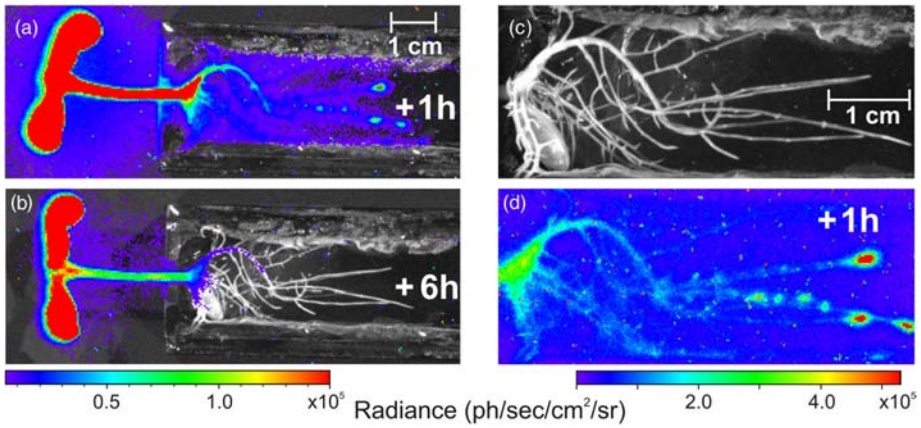


Figure 15. CLI and optical images of young cucumber plant labeled with $^{11}CO_2$: (a) 1 h post labeling; (b) 6 h post labeling; (c) photograph and (d) corresponding high resolution CLI image of the roots

## Conclusions

Using the combination of PET, simultaneous beta and coincidence-gamma imager, and CLI imaging, we have developed a robust framework for in vivo quantitative measurements of positron-emitting radionuclide such as $^{11}C$ and $^{13}N$ in plants. This unique capability enabled us to start a molecular plant phenotyping imaging program at the Washington University in St. Louis. We joined the Plant Imaging Consortium, a NIH-funded EPSCoR Track II program between the states of Arkansas and Missouri, in 2014. Together, we are promoting to use of advanced imaging technologies (including radiotracer imaging) to conduct plant research. This new initiative would not be possible without the DOE BER's funding.

## Publications:


(1) Wu H and Tai Y-C, A Novel Phoswich Imaging Detector for Simultaneous Beta and Coincidence-Gamma Imaging of Plant Leaves, Phys. Med. Biol.56: 5583-5598, 2011

(2) H Ranjbar, J Wen, AJ Mathews, S Komarov, Q Wang, K Li, JA O'Sullivan, Y-C Tai, A simultaneous beta and coincidence-gamma imaging system for plant leaves, Phys. Med. Biol. 61:3572-95 (2016); doi:10.1088/0031-9155/61/9/3572

(3) Komarov S, Zhou D, Liu Y, and **Tai Y-C**, Cherenkov luminescence imaging in transparent media and the imaging of thin or shallow sources, J. Biomed. Opt., 20(3), 036011 (2015). doi:10.1117/1.JBO.20.3.03601